Short-range order in ion irradiated fluorite structural derivatives in Sc2O3-HfO2

Takahiro Izumi, Masanari Iwasaki, Maulik K. Patel, Gianguido Baldinozzi, C. Grygiel, Manabu Ishimaru

Short-range order in ion irradiated fluorite structural derivatives in Sc_2O_3-HfO_2

Takahiro Izumi,[1] Masanari Iwasaki,[1] Maulik K. Patel,[2] Gianguido Baldinozzi,[3] Clara Grygiel,[4] and Manabu Ishimaru[1,*]

[1]*Department of Materials Science and Engineering, Kyushu Institute of Technology, Fukuoka 804-8550, Japan*

[2]*Department of Materials Design and Manufacturing, School of Engineering, The University of Liverpool, Liverpool L69 3GH, United Kingdom*

[3]*Structures, Propriétés et Modélisation des Solides, Université Paris-Saclay, CentraleSupelec, CNRS, 91190 Gif-sur-Yvette, France*

[4]*CIMAP, CEA-CNRS-ENSICAEN-UNICAEN, Bd. Henri Becquerel, Caen, France*

Abstract

Knowledge of radiation-induced structural changes in complex oxides is of technological importance for the development of container materials for the immobilization of nuclear waste. Fluorite structural derivatives are candidates for container materials, but their disordering processes under radiation environments are still unclear. In the present study, ion irradiation was performed on the Sc_2O_3-HfO_2 pseudo-binary system in which fluorite-related structural compounds such as β-$Sc_2Hf_7O_{17}$, γ-$Sc_2Hf_5O_{13}$, and δ-$Sc_4Zr_3O_{12}$ exist, and the short-range ordered structures were investigated by transmission electron microscopy (TEM). The pristine long-range ordered rhombohedral phase was found to transform into a long-range disordered cubic oxygen-deficient fluorite phase upon ion irradiation. The atomic arrangements are not completely disordered, but a more ordered structure was present in the disordered fluorite matrix. A characteristic diffuse scattering was observed in the electron diffraction patterns, and dark-field TEM observations revealed that it is due to microdomains, defined as small regions where the degree of order is higher than that of the disordered matrix. Although the parent phase was different before irradiation, the short-range organization is the same. A comparison of diffuse scattering with the location of superlattice reflections suggested that the microdomains have a structure similar to the δ-phase. With increasing Sc_2O_3 concentration, the microdomains of δ-type structures were suggested to change to short-range ordered bixbyite structures, which are not present in the

equilibrium phase diagram.

*Corresponding author: ishimaru@post.matsc.kyutech.ac.jp

1. Introduction

Mixed oxides consisting of two or more positively charged ions, so-called complex oxides, are attracting attention as candidate materials for the immobilization of nuclear waste [1-4], because they can incorporate actinides via a substitution mechanism. The decay of radioactive elements generates large amounts of heat and radiation. The energetic particles cause damage to the surrounding crystal structure, so materials for nuclear waste immobilization need to be not only thermally and chemically stable, but also radiation tolerance. Since structural changes such as amorphization and polymorphism are often induced by damage accumulation in these systems, knowledge of their structural and mechanical behavior under irradiation is of technological importance for establishing safer solutions for nuclear waste immobilization.

When cations in the parent fluorite structure are replaced with aliovalent cations, oxygen vacancies are created to satisfy the electroneutrality condition. The regular arrangements of vacancies and/or cations give rise to a variety of polyhedral and symmetries. Nevertheless, in fluorite-derived systems, some differences can be expected between processes involving the aliovalent cation ordering and the oxygen vacancy ordering as a result of their strongly asymmetric kinetic factors. Oxides with a fluorite-type structure, such as uranium dioxide and zirconium dioxide, exhibit excellent radiation resistance, and therefore the fluorite-related oxides are anticipated as possible container materials for immobilizing high-level nuclear waste. Irradiation often causes an order-to-disorder structural phase transformation in complex oxides [5-8], and the accumulation of defects and damage may eventually lead to amorphization. Radiation-induced amorphization can be predicted based on the Lindeman criteria [9] and the phase diagram [10], but the contingent formation of metastable crystalline phases, far from the equilibrium state, is a more difficult task. Also, simultaneous structural and local compositional changes occur at the atomistic scale. It has been pointed out that nanoscale phase separation may cause incongruent dissolution of the waste form, which may adversely affect our living environment [11].

Structural changes of compounds under radiation environments are expected to maintain a medium or a short-range organization before complete disorder. It has been pointed out that short-range order influences the kinetics behaviors of interstitials and vacancies created by irradiation [12], and therefore the

description of short-range order is of technological relevance for the design and engineering of radiation tolerant materials. Recent studies of the order-to-disorder phase transformation in pyrochlore oxides have shown that the atomic arrangements are not completely disordered, but exhibit a different type of local order (e.g., weberite-type structures) than previously thought [13-18]. Displacive and compositional fluctuations give rise to diffuse scattering in the diffraction patterns. The combination of transmission electron microscopy (TEM) and electron diffraction is a powerful technique for analyzing diffuse scattering. This is because the strong interaction of electrons with matter allows very weak scattering signals to be detected. In the fluorite-related materials, characteristic complex diffuse scattering patterns are observed in the solid solution systems ZrO_2-RE_2O_3 (RE: rare earth elements) [19-22], CeO_2-RE_2O_3 [19,23], and HfO_2-RE_2O_3 [22]. However, investigations of radiation-induced short-range order and local structures in these pseudo-binary systems are very limited.

The δ-type structure represented by the $A_4B_3O_{12}$ composition has excellent irradiation resistance: δ-$Sc_4Zr_3O_{12}$ does not amorphize even at high radiation doses exceeding 45 displacements per atom (dpa) [10]. We have studied the irradiation behavior of δ-$Sc_4Zr_3O_{12}$ [24] and δ-$Sc_4Hf_3O_{12}$ [25] and found that the short-range order is described by a bixbyite structure. Bixbyite is also a derivative of the fluorite structure, but the transformation to δ- bixbyite cannot occur continuously; it is reconstructive and involves a change in the interatomic bond topology: the transformation from the trigonal rhombohedral ordered δ-phase towards a cubic bixbyite structure involves an intermediate disordered cubic fluorite structure [24,25]. There are various ordered fluorite structural derivatives in the equilibrium Sc_2O_3-ZrO_2 and Sc_2O_3-HfO_2 pseudo-binary phase diagrams [26,27], and therefore these systems provide a playground for analyzing the structural changes and mechanisms associated with radiation-induced disorder. In the present study, we have examined the diffuse scattering associated with structural changes promoted by ion irradiation using TEM and electron diffraction techniques.

2. Experimental

Polycrystalline pellets of β-$Sc_2Hf_7O_{17}$ and γ-$Sc_2Hf_5O_{13}$ were synthesized by solid state synthesis, and then

surface-polished circular pellets (10 mm in diameter) were prepared for ion irradiation in the same way as for δ-$Sc_4Hf_3O_{12}$ [25,28]. In the present study, the pellets were irradiated with 600 keV Kr^{3+} ions to fluences ranging from 1×10^{14} to 5×10^{15} Kr^{3+}/cm^2 using a 200 kV Danfysik High Current Research Ion Implanter at the Ion Beam Laboratory in Los Alamos National Laboratory, USA. We have recently found that structural changes in ion irradiated δ-$Sc_4Hf_3O_{12}$ are induced by temperature rise [29]. To suppress the beam heating effects during irradiation, the specimens were irradiated with a flux of 1×10^{12} ions/cm^2s using a liquid nitrogen cooling stage. As a result, short-range ordered structures were successfully observed. For comparison, swift heavy ion irradiations were also performed with 93.6 MeV Pb^{28+} ions to a fluence of 5×10^{12} Pb^{28+} /cm^2 with a flux of 1.2×10^8 ions/cm^2s at room temperature using the IRRSUD beamline at GANIL (The Grand Accélérateur National d'Ions Lourds) in Caen, France. (Charge stripping is required for economical acceleration to higher energies, so Pb^{28+} ions were used for the swift heavy ion irradiation.)

Figure 1 shows the depth profiles of damage and projectile ions in (a) β-$Sc_2Hf_7O_{17}$ and (b) γ-$Sc_2Hf_5O_{13}$ irradiated with 600 keV Kr ions to a fluence of 5×10^{15} /cm^2, calculated in full-cascade simulations using SRIM-2008 [30]. The densities of β-$Sc_2Hf_7O_{17}$ and (b) γ-$Sc_2Hf_5O_{13}$ were set to 8.57 and 7.89 g/cm^3, respectively, and the threshold displacement energies were assumed to be 25 eV for Sc, 25 eV for Hf, and 28 eV for O. The damage and Kr distributions are almost comparable in the β- and γ-phases. The maximum concentration of Kr is 0.3 at.% at a depth of 200 nm, while the damage has a maximum value of 6.5 dpa at 110 nm. Note that the damage distribution predicted by SRIM is just an estimate of damage and sometimes deviates from the experimental data, especially for slow heavy ion irradiation, due to a significant overestimation of the electronic stopping power [31]. Thus, the SRIM results were used only for a qualitative estimation of the damage distribution.

Radiation-induced structural changes were examined by grazing incidence x-ray diffraction (GIXRD) and transmission electron microscopy (TEM). GIXRD profiles were obtained using a Rigaku Smart Lab operated at 40 kV and 200 mA with Cu $K\alpha$ radiation. For cross-sectional TEM observations, the pellets were cut using a diamond wheel saw, mechanically polished to a thickness of ~10 μm using a tripod polisher, and thinned to electron transparency by argon ion milling. To minimize ion milling damage, the

incident angle of the Ar beam was set to 5°, and the acceleration voltage was initially set at 4kV and then gradually reduced to 2kV. Under these conditions, the thickness of the damaged layer was estimated to be 3 nm by SRIM calculation (see the supplementary materials: Fig. S1). The TEM images and electron diffraction patterns were obtained from relatively thick regions of the TEM sample, so the effect of the very thin damage layer induced by ion milling is negligible. The ion milling was carried out using a liquid nitrogen cooling stage to suppress the effects of temperature rise on structure changes [29]. The specimens were observed using JEOL JEM-3000F and JEM-F200 operated at 300 and 200 kV, respectively. Images and electron diffraction patterns were recorded on imaging plates with high sensitivity, good linearity, and wide dynamic range for electron intensities [32]. Computer simulations of the electron diffraction patterns were performed using CrystalMaker and SingleCrystal (CrystalMaker Software, Ltd.).

3. Results and discussion

Figure 2 shows GIXRD profiles of (a) β-$Sc_2Hf_7O_{17}$ and (b) γ-$Sc_2Hf_5O_{13}$ irradiated with 600 keV Kr^{3+} ions at different ion fluences. The x-ray incident angle was fixed at 1°, and the corresponding penetration depths are ~340 nm for β and ~420 nm for γ. To make weak peaks easier to see, the intensity is plotted as a logarithm. In addition to the strong fundamental lattice reflections, weak superlattice reflections due to the ordering of the oxygen vacancies are observed in the pristine specimens. No structural data are available for the Sc_2O_3-HfO_2 system. Since the ionic radii are nearly identical for Hf^{4+} (0.058 nm) and Zr^{4+} (0.059 nm), the GIXRD profiles obtained here were compared with the x-ray diffraction profiles of β-$Sc_2Zr_7O_{17}$ (space group: $R\bar{3}$; a = 1.9817 nm, c = 1.8056 nm) [33] and γ-$Sc_2Zr_5O_{13}$ ($R\bar{3}$; a = 0.9474 nm, c = 1.7390 nm) [34]. The peak positions in the pristine samples are consistent with the simulated patterns calculated from the kinematical theory based on the previously reported model, shown on the abscissa axis. The superlattice peaks of the β-phase are weaker than those of the γ-phase, which is also consistent with the simulated diffraction intensities. The intensity of the superlattice reflections is significantly reduced with increasing the ion fluences, and the peak splitting and asymmetry around $2\theta = 30°$ and 50° disappear in the GIXRD for the β-phase. This suggests that an ordered rhombohedral-to-disordered cubic fluorite structural phase transformation occurs in the ion

irradiated β- and γ-phases.

It is difficult to discuss the radiation tolerance between β- and γ-phases from GIXRD alone, because the penetration depth of x-rays is approximately equal to or slightly greater than the end-of-range of projectile ions predicted by SRIM calculations (Fig. 1). To examine the structural changes as a function of the depth, cross-sectional TEM observations were performed. Figure 3 shows selected-area electron diffraction (SAED) patterns taken from (a,a') the damaged and (b,b') pristine regions of 5×10^{15} Kr^{3+}/cm^2 irradiated specimens: (a,b) β-$Sc_2Hf_7O_{17}$ and (a',b') γ-$Sc_2Hf_5O_{13}$. There are superlattice reflections in the patterns taken from the pristine regions. In Fig. 3(b), the superlattice spots can be interpreted as the superposition of (7 $\underline{11}$ 0) reciprocal lattice planes of the β-type structure with different variants. The pattern in Fig. 3(b') is consistent with that viewed along the $[\bar{1}4\bar{2}]$ direction of the γ-type structures. These superlattice reflections disappear and change to diffuse scattering due to radiation-induced order-to-disorder phase transformation. Very weak diffuse scattering was also observed in the diffraction patterns of Fig. 3(b), as indicated by the arrow, suggesting that the oxygen vacancy arrangements are not in a perfectly ordered state in the pristine samples.

Figure 3 shows cross-sectional dark-field TEM images of (c,d) β-$Sc_2Hf_7O_{17}$ and (c',d') γ-$Sc_2Hf_5O_{13}$ irradiated to a fluence of 5×10^{15} Kr^{3+}/cm^2. These images were taken by selecting (c,c') the fundamental lattice reflection and (d,d') the superlattice reflection in the vicinity of the transmitted beam. The damaged region exists from the surface to a depth of ~400 nm. Note that the surface of the β-$Sc_2Hf_7O_{17}$ in Fig. 3(c) is dark. This implies that the contribution of the fundamental lattice Bragg reflections is weaker in this region, suggesting poor crystallinity. Indeed, the amorphous phase and nanocrystallites were confirmed by high-resolution TEM observations (see the supplementary materials: Fig. S2). Although the irradiation conditions are identical, β-$Sc_2Hf_7O_{17}$ is more damaged than γ-$Sc_2Hf_5O_3$ (*cf.* Figs. 3(c) and 3(c')), suggesting that the β-phase is more susceptible to radiation damage than the γ-phase. It has been pointed out that the radiation-induced phase transformation resistance correlates with the long-range order-to-disorder phase transformation temperature of these compounds [35]. Since the β- and γ-phases polymorphs are structurally stable up to 680 ^{o}C and 850 ^{o}C, respectively [36], the radiation behavior observed here is

reasonable. In the dark-field images formed by superlattice reflection (Figs. 3(d) and 3(d')), the contrast of the surface region indicated by the double-headed arrow is darker than that of the substrate. The darker regions of the dark-field image indicate that the reflections used for imaging are very weak, suggesting a small contribution of superlattice reflections in the 400 nm depth region from the surface. In other words, the long-range order-to-disorder phase transformation is induced by irradiation damage.

The presence of remarkable diffuse scattering was detected by electron diffraction, as shown in Figs. 3(a) and 3(a'). To examine its distribution in the reciprocal space, the specimens were observed along different crystallographic directions. The diffraction patterns were taken from the ion irradiated regions without the surface damage observed in the dark-field images. Figure 4 shows the SAED patterns taken with an electron beam of ~100 nm diameter from the damage region of (a-f) β-$Sc_2Hf_7O_{17}$ and (a'-f') γ-$Sc_2Hf_5O_{13}$ irradiated to a fluence of 5×10^{15} Kr^{3+}/cm^2. The diffraction patterns are shown with inverted intensity to enhance the weak scattering features. The diffraction patterns are indexed in terms of the parent fluorite-type structure. The electron beam has different orientations in these patterns in Fig. 4: incident along (a,a') [100], (b,b') [110], (c,c') [111], (d,d') [310], (e,e') [112], and (f,f') [321] zone-axes of the fluorite-type structure. Although the pristine structures are different, the distribution of diffuse scattering is qualitatively the same for the ion irradiated β and γ phases. Weak diffuse streaks connecting the fundamental lattice spots along the [010] and [001] directions are observed in the (100) reciprocal lattice plane (Figs. 4(a) and 4(a')). This diffuse scattering feature is clearly visible in the diffraction pattern in Fig. 4(a'), which is slightly tilted from the [100] zone-axis. The SAED pattern viewed along the [110] direction also shows diffuse scattering connecting the fundamental lattice spots, but its shape is similar to an irregular lozenge tilting (Figs. 4(b) and 4(b')). In the (111) diffraction patterns, six diffuse scattering lines are seen extending from the fundamental lattice spot towards the nearest neighbor spots, forming a hexagonal flower-like pattern (Figs. 4(c) and 4(c')). Characteristic diffuse scattering with a ring-like morphology was observed at relatively higher incident directions, as shown in Figs. 4(d-f) and 4(d'-f'). The diffuse scattering intensity appears to decrease with increasing scattering vector.

The diffuse scattering on the (100), (110) and (111) reciprocal lattice planes is schematically

shown in Figs. 5(a), 5(b), and 5(c), respectively. Note that the diffuse scattering along the <110> directions is observed in the (110) pattern (Figs. 4(b,b')) and the (111) pattern (Figs. 4(c,c')), but not in the (100) pattern (Figs. 4(a,a')). This suggests that they appear due to double diffraction. Considering the diffraction patterns shown here and those described below (Fig. 10), a schematic diagram of diffuse scattering was constructed using Blender (free and open source software) [37], as shown in Fig. 5(d). As described above, the diffuse scattering features indicated by the arrows are not present in the {100}* planes passing through the origin of the reciprocal lattice space.

Characteristic diffuse scattering in the electron diffraction patterns has often been observed in fluorite-related solid solutions in which pyrochlore ($A_2B_2O_7$) [11,20,38-42] and bixbyite (*C*-type rare earth) (M_2O_3) [19,23,42] are mixed with the fluorite phase (MO_2). Diffuse scattering can arise from the atomic displacements, compositional modulations, and phase boundaries between ordered domains [43]. Since the long-range ordered β- and γ-phases were destroyed by ion irradiation, there is a compelling possibility that the diffuse scattering is a signature of short-range correlations in the long-range disordered phase. On closer examination of the dark-field TEM images, it was found that there are faint dots dispersed in the damaged region in Figs. 3(d) and 3(d'). Figures 6(a) and 6(b) show the enlarged views of the dashed square area in Figs. 3(d) and 3(d'), respectively. There is a spotty contrast with a correlation length of less than 2 nm. Considering the ion fluence of 5×10^{15} Kr^{3+}/cm^2, we can conclude that the individual cascades overlap: the spotty contrast is not due to residual unirradiated areas. The presence of the spotty contrast suggests that the ordered phase is not completely disordered by ion irradiation, but is in a short-range ordered state, which is responsible for the diffuse scattering. The dark-field images in Fig. 6 resemble the image of a microdomain [44]. Microdomains are defined as small regions where the degree of order is higher than that of the disordered matrix [45]. Their density seems to be greater in the ion irradiated γ-$Sc_2Hf_5O_{13}$ than in β-$Sc_2Hf_7O_{17}$. The fast Fourier transform (FFT) diagram of the high-resolution TEM image also detected weak scattering corresponding to diffuse scattering, as shown in the supplementary materials (Fig. S3). Its distribution is consistent with that observed in the SAED pattern, suggesting that the high-resolution image contains short-range order information: the existence of the microdomains was confirmed by high-resolution TEM

observations. However, the intensity of the scattering in the FFT diagram is very weak and the domain boundaries are unclear in the high-resolution TEM image. This suggests that the degree of order within the microdomains is low and it is difficult to extract further structural information from high-resolution TEM observations.

Diffuse scattering in diffraction patterns can also arise from dynamic atomic displacements, such as soft phonon modes [46-48]. To confirm whether the diffuse scattering observed in this study was due to thermal diffuse scattering, *in-situ* TEM observations were performed using a liquid nitrogen cooling holder. Figure 7 shows SAED patterns taken at (a-c) room temperature and (a'-c') -140 ºC. The electron beam was incident along the (a,a') [110], (b,b') [310], and (c,c') [321] directions. These patterns were recorded from the identical area, to avoid the thickness correlation effects on the diffraction intensities. Diffuse scattering is still observed and the intensities are not temperature dependent. This suggests that the origin of the diffuse scattering observed here is due to the short-range correlations with the ordered microdomain rather than to dynamic atomic vibration.

The shape and distribution of the diffuse scattering is very similar to that previously observed in CeO_2 with 22 mol.% Y_2O_3, but is not consistent with a microdomain structure with bixbyite domains dispersed in a fluorite-type matrix [23]. The diffuse scattering observed here was compared with an array of superlattice reflections to identify the microdomain structural organization, following the approach developed by other researchers [49-52]. As observed in the SAED patterns, there is a crystallographic orientation relationship between the pristine structures and the ion-induced fluorite structure. The following reflections overlap in the diffraction patterns of the rhombohedral ordered and cubic disordered phases.

$$11\,\bar{7}\,0_\beta = 2\,\bar{2}\,0_F, 7\,4\,0_\beta = 2\,0\,\bar{2}_F, 0\,0\,6_\beta = 1\,1\,1_F$$

$$\bar{1}\,\bar{4}\,0_\gamma = 2\,\bar{2}\,0_F, 5\,\bar{1}\,0_\gamma = 0\,2\,\bar{2}_F, 0\,0\,6_\gamma = 1\,1\,1_F$$

Thus, their crystal axes are related as follows:

$$a_\beta = \frac{1}{93}[22\,\bar{8}\,\overline{14}]_F, b_\beta = \frac{1}{93}[8\,14\,\overline{22}]_F, c_\beta = \frac{1}{6}[1\,1\,1]_F$$

$$a_\gamma = \frac{1}{21}[\bar{2}\,10\,\bar{8}]_F, b_\gamma = \frac{1}{21}[\overline{10}\,8\,2]_F, c_\gamma = \frac{1}{6}[1\,1\,1]_F$$

Based on this crystallographic relationship, the following crystal lattice transformation matrices are obtained:

$$\begin{pmatrix} a \\ b \\ c \end{pmatrix}_{\beta} = \frac{1}{93}\begin{pmatrix} 22 & -8 & -14 \\ 8 & 14 & -22 \\ 15.5 & 15.5 & 15.5 \end{pmatrix}\begin{pmatrix} a \\ b \\ c \end{pmatrix}_{F}$$

$$\begin{pmatrix} a \\ b \\ c \end{pmatrix}_{\gamma} = \frac{1}{42}\begin{pmatrix} -4 & 20 & -16 \\ -20 & 16 & 4 \\ 7 & 7 & 7 \end{pmatrix}\begin{pmatrix} a \\ b \\ c \end{pmatrix}_{F}$$

Here, the subscript *F* denotes the reference lattice of the fluorite structure. Since the experimental diffuse scattering is clearly observed in the <111>, <112>, and <310> zone-axes of the cubic fluorite structure, the simulated patterns were compared with these patterns. The structural models considered consist of overlapping variants with different oxygen vacancy arrangements. For example, the average cubic fluorite structure possesses twelve equivalent <112>-type zone-axes; the corresponding diffraction patterns of each rhombohedral ordered variant were calculated and merged using the above crystallographic relations. Figure 8 shows the simulated diffraction patterns of the rhombohedral ordered structure, taking into account the overlap of the different orientation variants, superimposed on the experimental SAED pattern obtained from the damaged region: (a1-c1) β-$Sc_2Hf_7O_{17}$ and (a2-c2) γ-$Sc_2Hf_5O_{13}$. The SAED patterns were chosen to have clearly visible diffuse scattering. The large and small blue circles represent the transmitted beam and cubic fluorite reflections common to all variants, respectively, while the red circles correspond to the combination of superlattice spots generated by the different orientation variants. It was found that the superlattice spots due to the γ-type pristine structure overlap with the diffuse scattering in the (111) and (112) diffraction patterns. However, there is no diffuse scattering in the dashed rectangular region of the (310) pattern (Fig. 8(c2)), although the corresponding superlattice reflections are relatively strong.

Another compound exists in the Sc_2O_3-HfO_2 pseudo-binary system, δ-$Sc_4Hf_3O_{12}$. This structure is also trigonal rhombohedral, but with a lattice ($a_\delta = a_\gamma$, $b_\delta = b_\gamma$, $c_\delta = c_\gamma/2$) that is just one half of the γ-phase one, due to the different oxygen vacancy ordering characteristics in these two compounds. The δ-phase gives rise to a superlattice spot distribution similar to that of the (111) and (112) reciprocal lattice planes of the γ-phase, as shown in Figs. 8(a3) and 8(b3), respectively. For a superlattice reflection distribution on the (310) reciprocal lattice plane, the δ-type structure reproduces the diffuse scattering features better than the γ-type structure. This suggests that the diffuse scattering arises from microdomain correlations with a δ-type

structure rather than with a β- or γ-type structure. Weak diffuse scattering was observed in the [100] and [110] zone-axes, but no superlattice reflections appear on these patterns if microdomains with δ-type structure and matrix with a bixbyite structure are always coherent. Gallardo-López *et al.* [50,51] observed diffuse scattering on the (110) reciprocal lattice plane in ZrO_2 with 24-32 mol% Y_2O_3, and reproduced them by considering the [211] and $[1\bar{1}\bar{1}]$ zone-axes of the δ-type structure. However, the diffuse scattering observed along these zone axes in the present study cannot be reproduced by microdomains where the oxygen vacancies order with correlations typical of the δ-type structure, suggesting that another family of microdomains with bixbyite-type structure must be involved in the model.

When irradiated with ions at keV energy, where knock-on effects are pronounced, the ion and damage distributions overlap, as shown in the SRIM calculations (Fig. 1). To avoid any chemical effects due to ion species, we performed swift heavy ion irradiations, where ionization effects are remarkable and ion species and damaged regions are clearly separated [28]. Figure 9 shows the GIXRD profiles of the pristine and 93.6 MeV Pb^{28+} ion irradiated (a) β-$Sc_2Hf_7O_{17}$ and (b) γ-$Sc_2Hf_5O_{13}$ to a fluence of 5×10^{12} /cm^2. The incident angle of the x-rays was set to 5° and the x-ray penetration depth was estimated to be ~1.4 μm for β and ~1.8 μm for γ. The superlattice reflections are visible in the pristine sample due to the greater penetration depth than in Fig. 2. The superlattice reflections disappear in the ion irradiated sample, suggesting that disordering occurs at least up to 1.5 μm from the surface. The SRIM simulation results in the inset indicate that electronic stopping power is dominant in this area. Electron diffraction patterns were therefore obtained from the <1.5 μm region. Figure 10 shows the SAED patterns taken from the irradiation-induced damage region of (a1-d1) β-$Sc_2Hf_7O_{17}$ and (a2-d2) γ-$Sc_2Hf_5O_{13}$. For comparison, the diffraction patterns of δ-$Sc_4Hf_3O_{12}$ irradiated with 92 MeV Xe^{26+} ions to a fluence of 1×10^{14} /cm^2 are also shown in Figs. 10(a3-d3), which was reported previously [25]. Due to the wide damage area produced by the swift heavy ion irradiation, the SAED patterns were recorded with an electron beam of ~400 nm diameter. As a result, diffuse scattering features were clearly observed. Their distribution and profile are qualitatively similar to those observed for keV ion irradiation, but closer examination reveals a slight difference between keV and MeV ion irradiated specimens. (To facilitate comparison, the diffraction patterns of the γ-phase irradiated with keV and MeV

ions are shown in the supplementary materials (Fig. S4)). Intensity maxima appear at the 110 and equivalent positions in the (100) diffraction pattern, as indicated by an arrow in Figs. 10(a1) and 10(a2). These intensity maxima around the fundamental lattice spot are observed in the (110) diffraction pattern of Figs. 10(b1) and 10(b2), but the amplitude of their modulation vector increases in the γ-phase compared to the β-phase. Notable qualitative differences were observed in the ring-shaped diffuse scattering between the β-$Sc_2Hf_7O_{17}$ and γ-$Sc_2Hf_5O_{13}$ compounds. Two types of ring-shaped diffuse scattering with different diameters exists in the (110) diffraction pattern, as indicated by the black and white double-headed arrows in Figs. 10(d1) and 10(d2). The diameter difference becomes smaller with increasing the Sc composition. We have previously found the formation of the metastable short-range ordered bixbyite phase in δ-$Sc_4Hf_3O_{12}$ irradiated with 92 MeV Xe^{26+} ions [25] and in δ-$Sc_4Zf_3O_{12}$ irradiated with 300 keV Kr^{2+} ions [24]. With increasing Sc concentration, the intensity maxima lock onto the position of the bixbyite superlattice reflections. As described above, the diffuse scattering in the (100) and (110) cannot be explained by the microdomains with the δ-type structures, whereas they can be reproduced by considering the bixbyite structure (see the distribution of the superlattice spots in the diffraction patterns of Figs. 10(a3-d3). These results suggest that the δ-type microdomains initially formed in the ion irradiated β and γ-phases are transformed into short-range bixbyite microdomains with the damage accumulation. The changes in the short-range ordered microdomains are summarized as follows:

β-$Sc_2Hf_7O_{17}$, γ-$Sc_2Hf_5O_{13}$ —(Knock-on effect, Ionization effect)→ δ-type microdomains —(Ionization effect)→ Bixbyite microdomains

δ-$Sc_4Zr_3O_{12}$ —(Knock-on effect, Ionization effect)→ Bixbyite microdomains

Diffuse scattering from microdomains with δ-type structure, as well as that from bixbyite-type microdomains, is observed in high-energy ion irradiated specimens where ionization is dominant. On the other hand, only diffuse scattering from microdomains with δ-type structure is observed in low-

energy ion irradiated samples with a pronounced knock-on effect. The difference between the two is not yet clear. Since the bixbyites have also been observed in the low-energy ion irradiated δ-phase [24], they may be produced in the low-energy ion irradiated β- and γ-phases by introducing higher levels of damage.

Shamblin *et al.* [13,14] studied the disordering processes of the ordered pyrochlores (space group: $Fd\bar{3}m$) by atomic pair-distribution function analysis using neutron diffraction, and found the formation of an orthorhombic weberite-type structure (*Ccmm*), another derivative of the fluorite structure. The ideal pyrochlore structure is represented by $A_2B_2O_7$, where an A-site cation (Wyckoff notation: 16*d*) is coordinated by eight nearest neighbor anions (six O at 48*f* and two O at 8*b*), while a B-site cation (16*c*) is surrounded by six O atoms and two vacancies (8*a*). The weberite-type structure is also represented as $A_2B_2O_7$, with a 7-coordinated cation (8*g*) in addition to 6-coordinated (4*a*) and 8-coordinated (4*b*) cations. Contrary to the system we have studied, the two types of cations in the pyrochlore and weberite structures exhibit a very strong site selectivity, with the A-type cation always occupying the 8-coordinated distorted cube environment and the B-type cation always occupying the octahedron. The different local structures and symmetries observed in the systems studied by Shamblin *et al.* [13,14] are driven by the different correlations occurring at the 7-fold coordinated sites. No such site selectivity is observed in the Sc_2O_3-HfO_2 and Sc_2O_3-ZrO_2 systems, since the variance between the ionic radii of Sc and Hf or Zr is at least one order of magnitude smaller than in pyrochlores. Our present study has also shown that ion irradiation leads to the formation of short-range ordered phases, which are different from those of the pristine compounds, but are mostly characterized by the ordering of oxygen vacancies and not by the short-range order involving the cation sites. Therefore, the disordering processes of the fluorite structural derivatives in Sc_2O_3-HfO_2, *i.e.* β-$Sc_2Hf_7O_{17}$, γ-$Sc_2Hf_5O_{13}$, and δ-$Sc_4Hf_3O_{12}$, are quite different from the pyrochlore and weberite structures. Indeed, the bixbyite-type structure represented by $(A,B)_2O_{3+x}$ can only occur if the A and B cations do not exhibit any pronounced site selectivity. Our previous studies using energy-dispersive x-ray spectroscopy, Rutherford backscattering spectroscopy, and x-ray photoelectron spectroscopy suggested that no compositional changes from the pristine phase occur [53]. While the formation of bixbyite can be rationalized using the concept of cation

radius variance, more extensive studies are still underway to understand the elementary mechanisms involved in the transformation steps leading to the bixbyite-type structures in these compounds.

The diffuse scattering observed here can be approximately reproduced on the basis of the δ-type ordered structure, but more accurate models need to take modulated structures into account [21,39,42]. As described above, there is no diffuse scattering in the [110] and equivalent directions through the origin of the reciprocal lattice, suggesting the presence of atomic displacements in transverse modes along the <110> directions. A detailed structural model has not yet been constructed, and extensive studies are currently underway.

4. Conclusions

Radiation-induced structural changes of β-$Sc_2Hf_7O_{17}$ and γ-$Sc_2Hf_5O_{13}$ were investigated by GIXRD and cross-sectional TEM. The ordered rhombohedral structure was confirmed to transform into the long-range disordered cubic fluorite structure upon ion irradiation. The β-phase is more susceptible to radiation damage than the γ-phase, and this behavior can be explained by the order-to-disorder polymorphic phase transformation temperature in their equilibrium phase diagrams. Diffuse scattering due to microdomains was observed in the electron diffraction patterns taken from the damaged region. The distribution of diffuse scattering in the reciprocal lattice space is similar in the β- and γ-phases, suggesting that the short-range ordered structure is independent of the pristine structure. The diffuse scattering distribution occurs near the location of superlattice reflections characteristic of the δ-phase structures, suggesting that the irradiation-induced microdomains have a short-range ordered organization related to the δ-phase polymorph, which is the most stable at high temperature in the equilibrium phase diagram. Evidence was found for the formation of short-range ordered bixbyite microdomains upon irradiation, a structural organization not present in the equilibrium Sc_2O_3-HfO_2 phase diagram. This metastable phase is most readily formed in compounds with increasing Sc concentration and damage accumulation.

Acknowledgements

This work was supported by JKA and its promotion funds from KEIRIN RACE (2023M-310), Kazuchika Okura Memorial Foundation, and JSPS KAKENHI Grant Number 24K01164 (MI). The GIXRD measurements were performed at the Center for Instrumental Analysis, Kyushu Institute of Technology and would like to thank Mr. Katsumi Yamamoto for his assistance. We would like to thank GANIL and CIMAP allocating the beamtime for irradiation on the IRRSUD beamline (experiment number P1052) and for their support in performing irradiations. We would like to thanks Dr. Yongqiang Wang for his assistance in performing the low energy irradiations using the Danfysik High Current Research Ion Implanter at the Ion Beam Laboratory in Los Alamos National Laboratory.

References

[1] W. J. Weber, R. C. Ewing, C. R. A. Catlow, T. Diaz de la Rubia, L. W. Hobbs, C. Kinoshita, Hj. Matzke, A. T. Motta, M. Nastasi, E. K. H. Salje, E. R. Vance, and S. J. Zinkle, Radiation effects in crystalline ceramics for the immobilization of high-level nuclear waste and plutonium, J. Mater. Res. 13 (1998) 1434-1484.

[2] R. C. Ewing, W. J. Weber, and J. Lian, Nuclear waste disposal - pyrochlore ($A_2B_2O_7$): Nuclear waste form for the immobilization of plutonium and "minor" actinides, J. Appl. Phys. 95 (2004) 5949-5971.

[3] W. J. Weber, A. Navrotsky, S. Stefanovsky, E. R. Vance, and E. Vernaz, Materials science of high-level nuclear waste immobilization, MRS Bulletin 34 (2009) 46-53.

[4] K. E. Sickafus, L. Minervini, R. W. Grimes, J. A. Valdez, M. Ishimaru, F. Li, K. J. McClellan, and T. E. Hartmann, Radiation tolerance of complex oxides, Science 289 (2000) 748-751.

[5] K. E. Sickafus, A. C. Larson, N. Yu, M. Nastasi, G. W. Hollenberg, F. A. Garner, and R. C. Bradt, Cation disorder in high dose, neutron-irradiated spinel, J. Nucl. Mater. 219 (1995) 128-134.

[6] G. R. Lumpkin, K. L. Smith, and M. G. Blackford, Heavy ion irradiation studies of columbite, brannerite, and pyrochlore structure types, J. Nucl. Mater. 289 (2001) 177-187.

[7] J. Lian, J. Chen, L. M. Wang, R. C. Ewing, J. Matt Farmer, L. A. Boatner, and K. B. Helean, Radiation-induced amorphization of rare-earth titanate pyrochlores, Phys. Rev. B 68 (2003) 134107 (9 pages).

[8] J. Lian, L. M. Wang, R. C. Ewing, S. V. Yudintsev, and S. V. Stefanovsky, Ion-beam-induced amorphization and order-disorder transition in the murataite structure, J. Appl. Phys. 97 (2005) 113536 (8 pages).

[9] P. R. Okamoto, N. Q. Lam and L. E. Rein, "Physics of Crystal-to-Glass Transformations", Solid State Physics, vol. 52, eds. H. Ehrenreich and F. Spaepen (Academic Press, San Diego, 1999).

[10] K. E. Sickafus, R. W. Grimes, J. A. Valdez, A. Cleave, M. Tang, M. Ishimaru, S. M. Corish, C. R. Stanek, and B. P. Uberuaga, Radiation-induced amorphization resistance and radiation tolerance in structurally related oxides, Nature Mater. 6 (2007) 217-223.

[11] D. P. Reid, M. C. Stennett, and N. C. Hyatt, The fluorite related modulated structures of the $Gd_2(Zr_{2-}$

$_x$Ce$_x$)O$_7$ solid solution: An analogue for Pu disposition, J. Solid State Chem. 191 (2012) 2-9.

[12] P. Cao, How does short-range order impact defect kinetics in irradiated multiprincipal element alloys?, Acc. Mater. Res. 2 (2021) 71-74.

[13] J. Shamblin, M. Feygenson, J. Neuefeind, C. L. Tracy, F. Zhang, S. Finkeldei, D. Bosbach, H. Zhou, R. C. Ewing, and M. Lang, Probing disorder in isometric pyrochlore and related complex oxides, Nature Mater. 15 (2016) 507-511.

[14] J. Shamblin, C. L. Tracy, R. I. Palomares, E. C. O'Quinn, R. C. Ewing, J. Neuefeind, M. Feygenson, J. Behrens, C. Trautmann, M. Lang, Similar local order in disordered fluorite and aperiodic pyrochlore structures, Acta Mater. 144 (2018) 60-67.

[15] R. Sherrod, E. C. O'Quinn, I. M. Gussev, C. Overstreet, J. Neuefeind, and M. K. Lang, Comparison of short-range order in irradiated dysprosium titanates, npj Mater. Degrad. 5 (2021) 19 (7 pages).

[16] E. C. O'Quinn, J. L. Bishop, R. Sherrod, J. Neuefeind, S. M. Montemayor, A. F. Fuentes, and M. Lang, Advanced characterization technique for mechanochemically synthesized materials: neutron total scattering analysis, J. Mater. Sci. 53 (2018) 13400–13410.

[17] I. M. Gussev, E. C. O'Quinn, G. Baldinozzi, J. Neuefeind, R. C. Ewing, F. Zhang, and M. Lang, Local order of orthorhombic weberite-type Y_3TaO_7 as determined by neutron total scattering and density functional theory calculations, Acta Mater. 196 (2020) 704-709.

[18] F. P. Marlton, Z. Zhang, Y. Zhang, T. E. Proffen, C. D. Ling, and B. J. Kennedy, Lattice disorder and oxygen migration pathways in pyrochlore and defect-fluorite oxides, Chem. Mater. 33 (2021) 1407-1415.

[19] R. L. Withers, J. G. Thompson, N. Gabbitas, L. R. Wallenberg, and T. R. Welberry, Microdomains, solid solutions and the "defect fluorite" to C-type sesquioxide transition in CeO_2-$RO_{1.5}$ and ZrO_2-$RO_{1.5}$ systems, J. Solid State Chem. 120 (1995) 290-298.

[20] Y. Tabira, R. L. Withers, J. C. Barry, and L. Elcoro, The strain-driven pyrochlore to "defect fluorite" phase transformation in rare earth sesquioxide stabilized cubic zirconias, J. Solid State Chem. 159 (2001) 121-129.

[21] S. Suzuki, M. Tanaka, and M. Ishigame, Structural studies on ZrO_2-Y_2O_3 system by electron diffraction and electron microscopy I, Jpn. J. Appl. Phys. 24 (1985) 401-410.

[22] S. Suzuki, M. Tanaka, and M. Ishigame, J. Phys. C: Solid State Phys. 20 (1987) 2963-2972.

[23] R. Wallenberg, R. Withers, D. J. M. Bevan, J. G. Thompson, P. Barlow, and B. G. Hyde, The fluorite-related "solid solutions" of CeO_2-Y_2O_3 I: A re-examination by electron microscopy and diffraction, J. Less-Common Met. 156, 1-16 (1989).

[24] M. Ishimaru, Y. Hirotsu, M. Tang, J. A. Valdez, and K. E. Sickafus, Ion-beam-induced phase transformations in δ-$Sc_4Zr_3O_{12}$, J. Appl. Phys. 102, 063532 (7 pages) (2007).

[25] M. Iwasaki, Y. Kanazawa, D. Manago, M. Patel, G. Baldinozzi, Kurt E. Sickafus, and M. Ishimaru, Anomalous structural phase transformation in swift heavy ion-irradiated δ-$Sc_4Hf_3O_{12}$, J. Appl. Phys. 132 (2022) 075901 (8 pages).

[26] H. M. Ondik and H. F. McMurdie, Phase Diagrams for Zirconium and Zirconia Systems, American Ceramic Society, Columbus (1998).

[27] G. A. Kalinovskaya, F. M. Spiridonov, and L. X. Komissarova, Phase equilibria in the system HfO_2-Sc_2O_3, J. Less-Common Met. 17 (1965) 151-159.

[28] M. K. Patel, K. E. Sickafus, and G. Baldinozzi, Divergent short- and long-range behavior in ion-irradiated δ-$Sc_4Hf_3O_{12}$, Phys. Rev. Mater. 4 (2020) 093605 (9 pages).

[29] M. Iwasaki, M. K. Patel, G. Baldinozzi, Kurt E. Sickafus, and M. Ishimaru, Stability of ion-beam-induced bixbyite phase in δ-$Sc_4Hf_3O_{12}$ under heat treatments and electron beam irradiations, J. Eur. Ceram. Soc. 44 (2024) 3131-3138.

[30] J. F. Ziegler, J. P. Biersack, and U. Littmark, The Stopping and Range of Ions in Solids (Pergamon, New York, 1985); available at http://www.srim.org.

[31] Y. Zhang, I.-T. Bae, K. Sun, C. M. Wang, M. Ishimaru, Z. Zhu, W. Jiang, and W. J. Weber, Damage profile and ion distribution of slow heavy ions in compounds, J. Appl. Phys. 105 (2009) 104901(12 pages).

[32] N. Mori, T. Oikawa, T. Katoh, J. Miyahara, and Y. Harada, Application of the "imaging plate" to TEM

image recording, Ultramicroscopy 25 (1988) 195-201.

[33] K. Wurst, E. Schweda, D. J. M. Bevan, J. Mohyla, K. S. Wallwork, and M. Hofmann, Single-crystal structure determination of $Zr_{50}Sc_{12}O_{118}$, Solid State Sci. 5 (2003) 1491-1497.

[34] F. M. Spiridonov, L. N. Popova, and R. Ya. Popil'skii, On the phase relations and the electrical conductivity in the system ZrO_2-Sc_2O_3, J. Solid State Chem. 2 (1970) 430-438.

[35] J. Zhang, Y. Q. Wang, J. A. Valdez, M. Tang, J. Won, and K. E. Sickafus, Ion irradiation-induced phase transformations in δ-γ-β phases of Sc_2O_3–ZrO_2 mixtures, Nucl. Instrum. Meth. Phys. Res. B 272 (2012) 244-248.

[36] A. V. Zyrin, V. P. Red'ko, L. M. Lopato, A. V. Shevchenko, I. M. Maister, and Z. A. Zaitseva, Ordered phase in the systems ZrO_2-Sc_2O_3 and HfO_2-Sc_2O_3, Izvestiya Akademii nauk SSSR. Neorganicheskie Mmaterialy (Inorganic Materials). 23 (1987) 1325-1329 (in Russian).

[37] https://www.blender.org

[38] M. P. Van Dijk, F. C. Mijlhoff, and A. J. Burggraaf, Pyrochlore microdomain formation in fluorite oxides, J. Solid State Chem. 62 (1986) 377-385.

[39] S. Esmaeilzadeh, J. Grins, and A.-K. Larsson, An electron and x-ray powder diffraction study of the defect fluorite structure of $Mn_{0.6}Ta_{0.4}O_{1.65}$, J. Solid State Chem. 145 (1999) 37-49.

[40] Y. Liu, R. L. Withers, L. Norén, The pyrochlore to 'defect fluorite' transition in Y2(ZryTi1-y)2O7 system and its underlying crystal chemistry, J. Solid State Chem. 177 (2004) 4404-4412.

[41] Y. Tabira and R. L. Withers, J. Solid State Chem. 148 (1999) 205-214.

[42] S. García-Martín, M. A. Alario-Franco, D. P. Fagg, and J. T. S. Irvine, Evidence of three types of short range ordered fluorite structure in the $(1-x)Y_{0.15}Zr_{0.85}O_{1.93}$ - $xY_{0.75}Nb_{0.25}O_{1.75}$ ($0 \leq x \leq 1$) system, J. Mater. Chem. 15 (2005) 1903–1907.

[43] J. L. Wardini, H. Vahidi, H. Guo, and W. J. Bowman, Probing multiscale disorder in pyrochlore and related complex oxides in the transmission electron microscope: A review, Front. Chem. 9 (2021) 743025 (27 pages).

[44] S. K. Das, P. R. Okamoto, P. M. J. Fisher, and G. Thomas, Short range order in Ni-Mo, Au-Cr, Au-V

and Au-Mn alloys, Acta Metall. 21 (1973) 913-928.

[45] W. M. Stobbs and J.-P. A. A. Chevalier, The classification of short range order by electron microscopy, Acta Metall. 26 (1978) 233-240.

[46] S. M. Shapiro, B. X. Yang, Y. Noda, L. E. Tanner, D. Schryvers, Neutron-scattering and electron-microscopy studies of the premartensitic phenomena in Ni_xAl_{100-x} alloys, Phys. Rev. B 44 (1991) 9301-9313.

[47] Y. Koyama and M. Ishimaru, Structural transitions in the superconducting oxides Ba-Pb-Bi-O, Phys. Rev. B 45 (1992) 9966-9975.

[48] C. Stock, D. Ellis, I. P. Swainson, G. Xu, H. Hiraka, Z. Zhong, H. Luo, X. Zhao, D. Viehland, R. J. Birgeneau, and G. Shirane, Damped soft phonons and diffuse scattering in 40% $Pb(Mg_{1/3}Nb_{2/3})O_3$-60% $PbTiO_3$, Phys. Rev. B 73 (2006) 064107 (12 pages).

[49] J. G. Allpress and H. J. Rossell, A microdomein description of defective fluorite-type phases $Ca_xM_{1-x}O_{2-x}$ (M=Zr, Hf; x=0.1-0.2), J. Solid State Chem. 15, 68-78 (1975).

[50] A. Gallardo-López, J. Martíez-Fernández, A. Domínguez-Rodríguez, and F. Ernst, Origin of diffuse electron scattering in yttria-cubic-stabilized zirconia single crystals with 24-32 mol% yttria, Phios. Mag. A 81 (2001) 1675-1689.

[51] A. Gallardo-López, J. Martíez-Fernández, and A. Domínguez-Rodríguez, Contribution to the study of the transition to a superstructure in high yttria content YCSZ, J. Eur. Ceram. Soc. 22 (2002) 2821-2825.

[52] M. C. Pienkowski, M. L. Jenkins, and P. T. Moseley, Microdomains in urania-yttria and urania-ceria, J. Solid State Chem. 92 (1991) 543-564.

[53] K. E. Sickafus, M. Ishimaru, Y. Hirotsu, I. O. Usov, J. A. Valdez, P. Hosemann, A. L. Johnson, and T. T. Thao, Compositional analyses of ion-irradiation-induced phases in δ-$Sc_4Zr_3O_{12}$, Nucl. Instrum. Meth. Phys. Res. B 266 (2008) 2892-2897.

Figure captions

Figure 1. The distribution of damage (red) and projectiles (blue) in (a) β-$Sc_2Hf_7O_{17}$ and (b) γ-$Sc_2Hf_5O_{13}$ irradiated with 600 keV Kr ions to a fluence of $5x10^{15}$ /cm^2, calculated by Monte Carlo simulations using SRIM2008.

Figure 2. GIXRD profiles of pristine and 600 keV Kr ion irradiated (a) β-$Sc_2Hf_7O_{17}$ and (b) γ-$Sc_2Hf_5O_{13}$ as a function of ion fluences. The incident angle of x-rays was fixed to 1°. The vertical axis is plotted on a logarithmic scale to enhance weak superlattice reflections. The lines on the abscissa axis indicate the peak positions of the β- and γ-type structures. The superlattice reflections become weak or disappear with increasing ion fluences, suggesting that the ordered rhombohedral phase is transformed into the disordered cubic fluorite phase.

Figure 3. SAED patterns taken from (a,a') the damage and (b,b') pristine regions of the specimens irradiated with 600 keV Kr^{3+} ions to a fluence of 5×10^{15} Kr^{3+}/cm^2: (a,b) β-$Sc_2Hf_7O_{17}$ and (a',b') γ-$Sc_2Hf_5O_{13}$. The patterns taken from the pristine regions correspond to (a) [7 $\underline{11}$ 0] and (b) $[\bar{1}4\bar{2}]$ zone-axes of β- and γ-type structures, respectively. Superlattice reflections in (a) and (b) disappear by ion irradiation, and the patterns transform to (a') $[\,11\,\bar{2}]$ and (b') $[\overline{21}\,\bar{6}\,3]$ zone-axis patterns of the fluorite-type structure. Cross-sectional dark-field TEM images of (c,d) β-$Sc_2Hf_7O_{17}$ and (c',d') γ-$Sc_2Hf_5O_{13}$. These images were taken by using (c,c') the fundamental lattice and (d,d') superlattice reflections.

Figure 4. SAED patterns taken from the damage regions of (a-f) β-$Sc_2Hf_7O_{17}$ and (a'-f') γ-$Sc_2Hf_5O_{13}$ irradiated with 600 keV Kr^{3+} ions to a fluence of 5×10^{15} Kr^{3+}/cm^2 with various electron beam incidence: (a,a') [100], (b,b') [110], (c,c') [111], (d,d') [310], (e,e') [112], and (f,f') [321] directions of the fluorite-type structure. In addition to the fundamental lattice spots, diffuse scatterings are present in the SAED patterns.

Figure 5. Schematic diagram of diffuse scattering distribution in the reciprocal lattice space observed by (a)

[100], (b) [110], and (c) [111] zone-axis. For clarity, the spacing of the fundamental lattice reflections is not matched in each schematic. (d) Three-dimensional distribution of the diffuse scatterings. The scattering marked by arrows is not observed on the {100}* plane including the origin of the reciprocal lattice space.

Figure 6. Magnified dark-field TEM images of the squared region in Fig. 3. (a) β-$Sc_2Hf_7O_{17}$ and (b) γ-$Sc_2Hf_5O_{13}$. Faint bright dots corresponding to microdomain are dispersed in the damaged region.

Figure 7. SAED patterns taken from the damage region of β-phase, recorded by *in situ* TEM at (a-c) room temperature and (a'-c') -140 ºC: (a,a') [110], (b,b') [310], and (c,c') [321] zone-axes. There is no noticeable difference in the intensity of diffuse scattering at different temperatures, suggesting that the origin of the diffuse scattering is not due to dynamical atomic displacements.

Figure 8. Overlay of experimental and simulated diffraction patterns of (a1-a1) [111], (b1-b3) [112], and (c1-c3) [310] zone-axes. The experimental diffraction patterns were taken from the damaged region. The simulated patterns were calculated by considering the variants of (a1-c1) β-$Sc_2Hf_7O_{17}$, (a2-c2) γ-$Sc_2Hf_5O_{13}$, and (a3-c3) δ-$Sc_4Hf_3O_{12}$. Blue circles denote the fundamental lattice spots due to fluorite-type structure, whereas red ones represent the superlattice spots due to oxygen vacancy ordering.

Figure 9. GIXRD profiles of pristine and 93.6 MeV Pb ion irradiated (a) β-$Sc_2Hf_7O_{17}$ and (b) γ-$Sc_2Hf_5O_{13}$. The incident angle of x-rays was set to 5º. Due to the large volume contributing to the x-ray diffraction, the superlattice peaks are more visible in the pristine samples than those of Fig. 2. The superlattice peaks disappear in the irradiated samples, indicating the order-to-disorder phase transformation. The electronic (S_e) and nuclear (S_n) stopping powers and their ratio (S_e/S_n) as a function of the depth, calculated by SRIM, are shown as the inset.

Figure 10. SAED patterns taken from the damage region of (a1-d1) β-$Sc_2Hf_7O_{17}$ and (a2-d2) γ-$Sc_2Hf_5O_{13}$

irradiated with 93.6 MeV Pb^{28+} ions to a fluence of 5×10^{12} /cm^2 and (a3-d3) δ-$Sc_4Hf_3O_{12}$ irradiated with 92 MeV Xe^{26+} ions to a fluence of 1×10^{14} /cm^2. The electron beam was incident along (a1-a3) the [100], (b1-b3) [110], (c1-c3) [111], and (d1-d3) [112] directions. Note that the superlattice spots in (a3-d3) are due to the bixbyite structure.

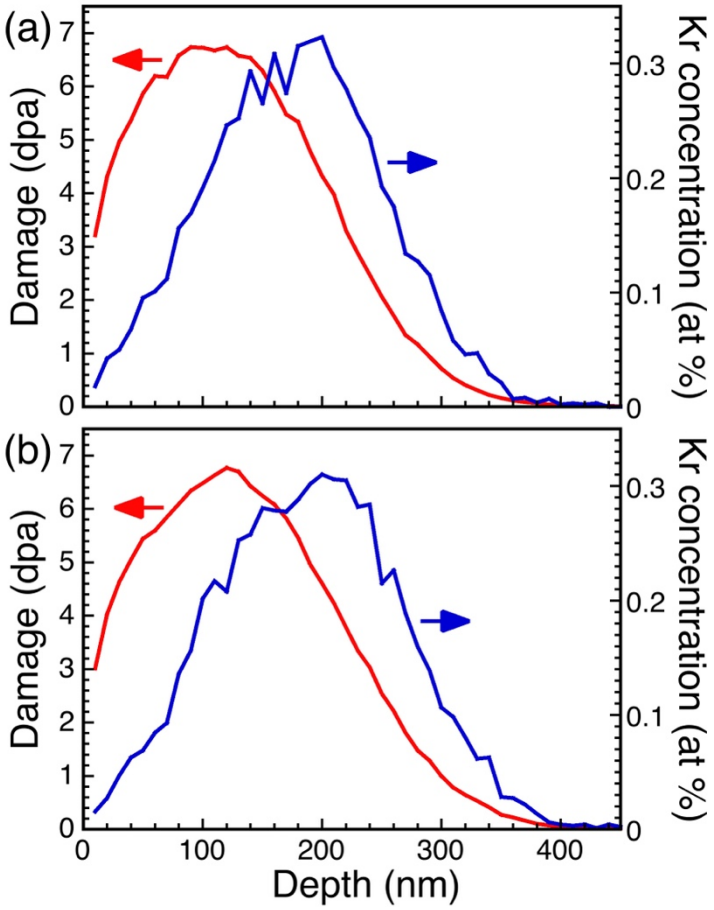
(a)
(b)
Damage (dpa)
Kr concentration (at %)
Depth (nm)
0
1
2
3
4
5
6
7
0.1
0.2
0.3
100
200
300
400

FIG. 1

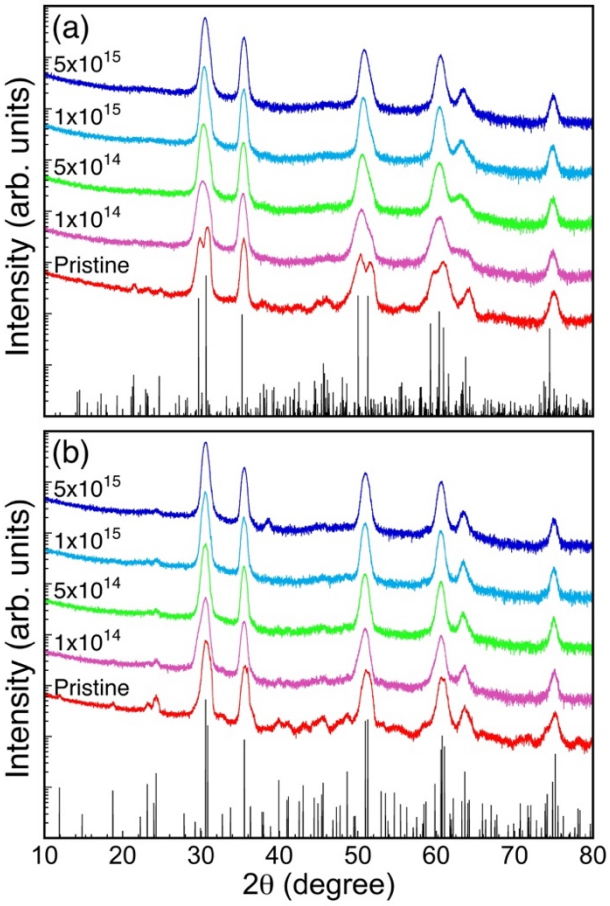
(a)
5x10^15
1x10^15
5x10^14
1x10^14
Pristine
Intensity (arb. units)
(b)
5x10^15
1x10^15
5x10^14
1x10^14
Pristine
Intensity (arb. units)
10
20
30
40
50
60
70
80
2θ (degree)

FIG. 2

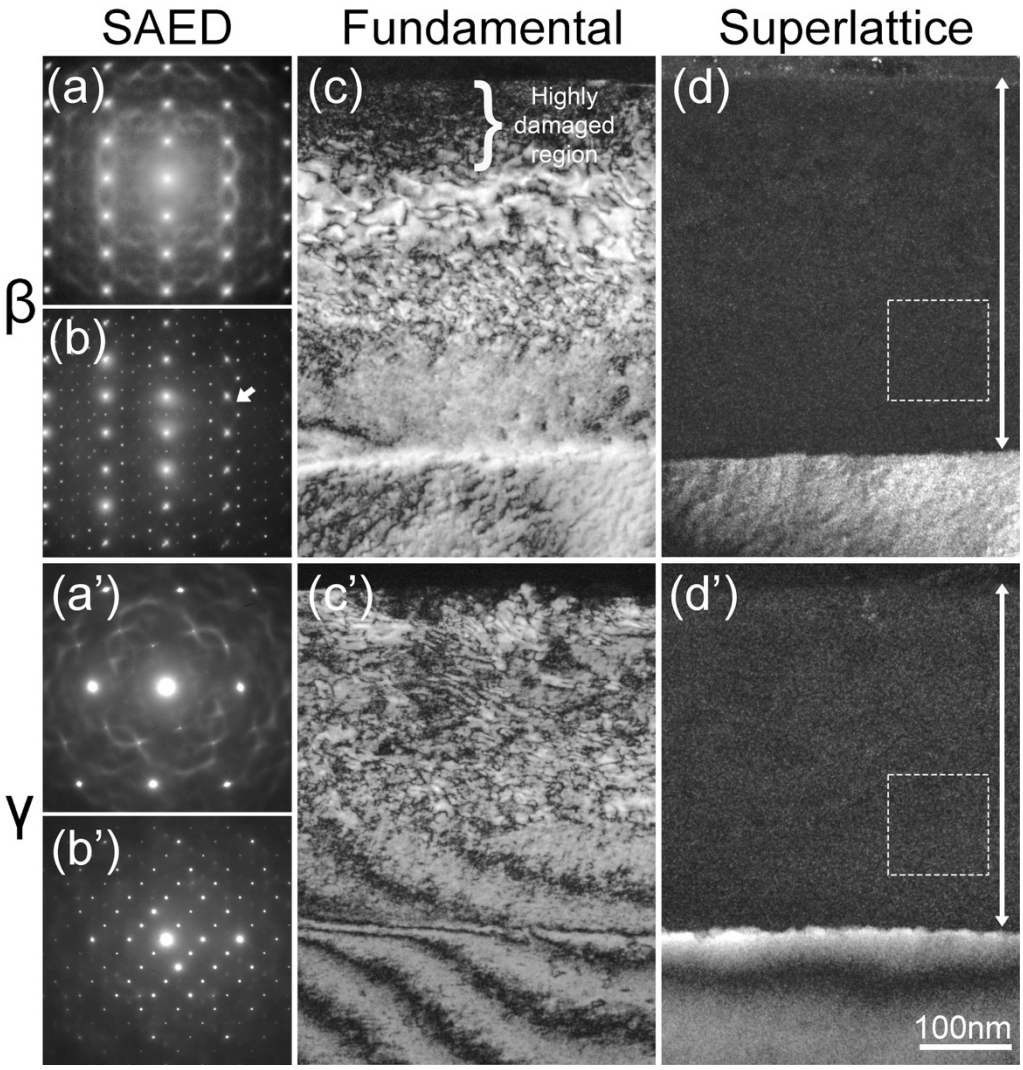
SAED
Fundamental
Superlattice
(a)
(b)
(c)
Highly damaged region
(d)
β
(a')
(b')
(c')
(d')
γ
100nm

FIG. 3

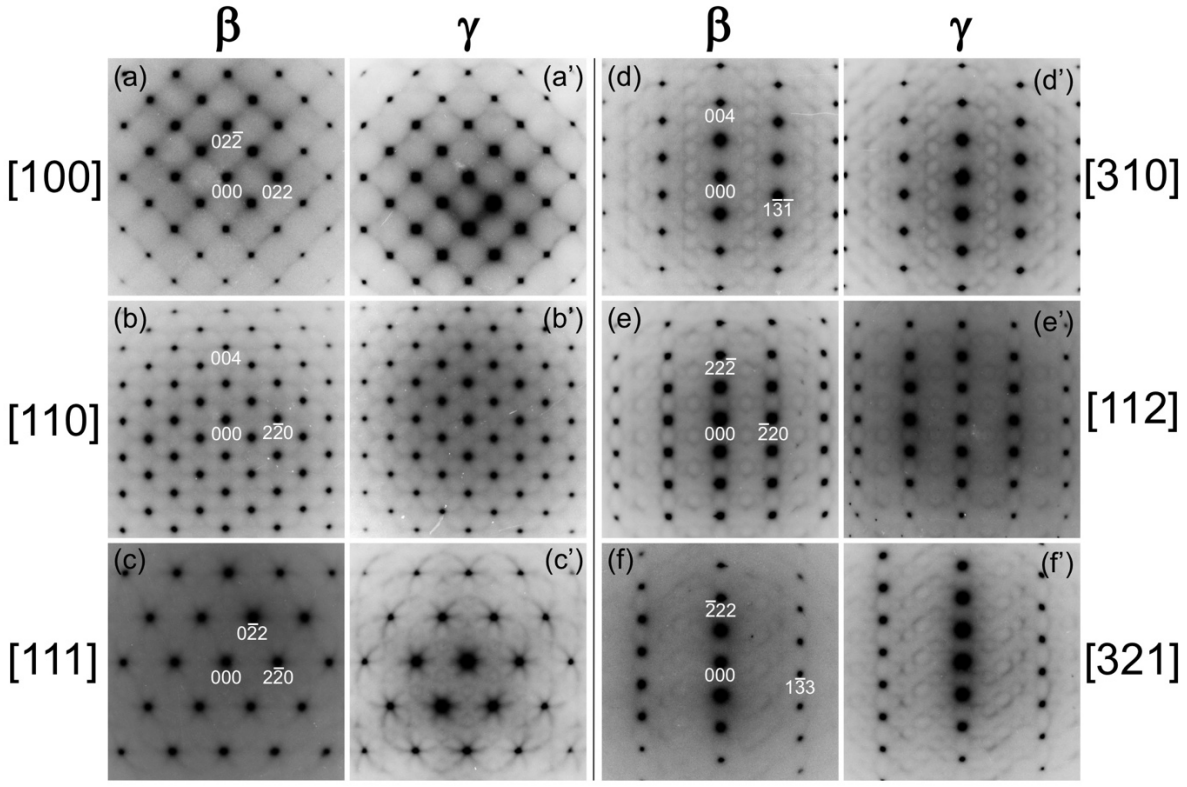

FIG. 4

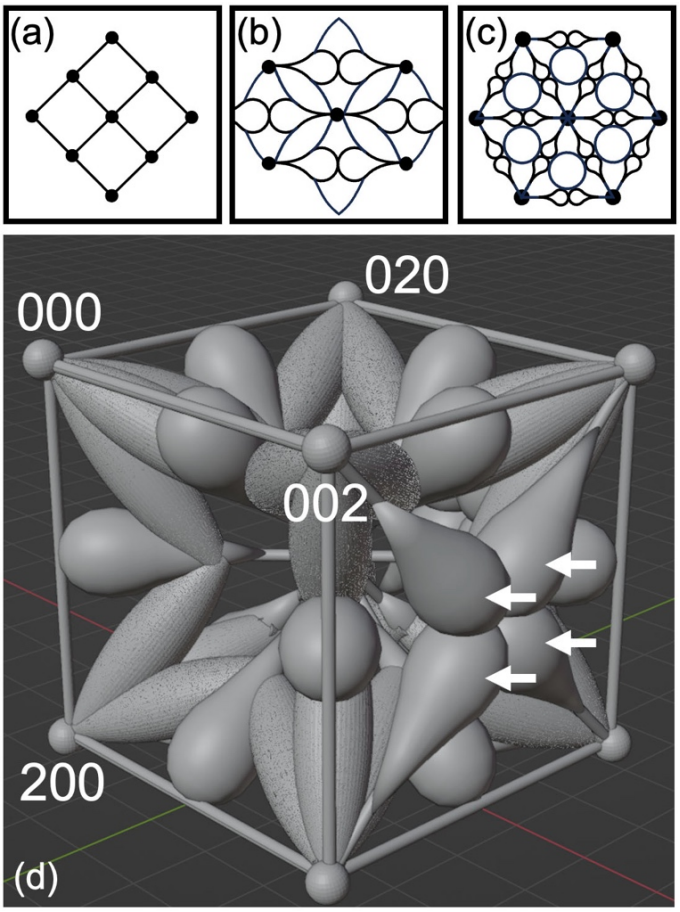

FIG. 5

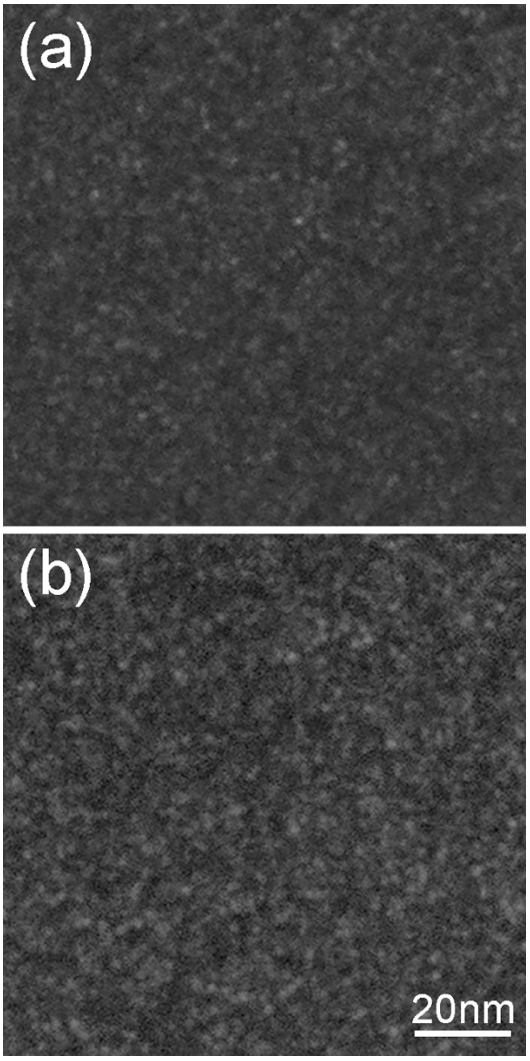

FIG. 6

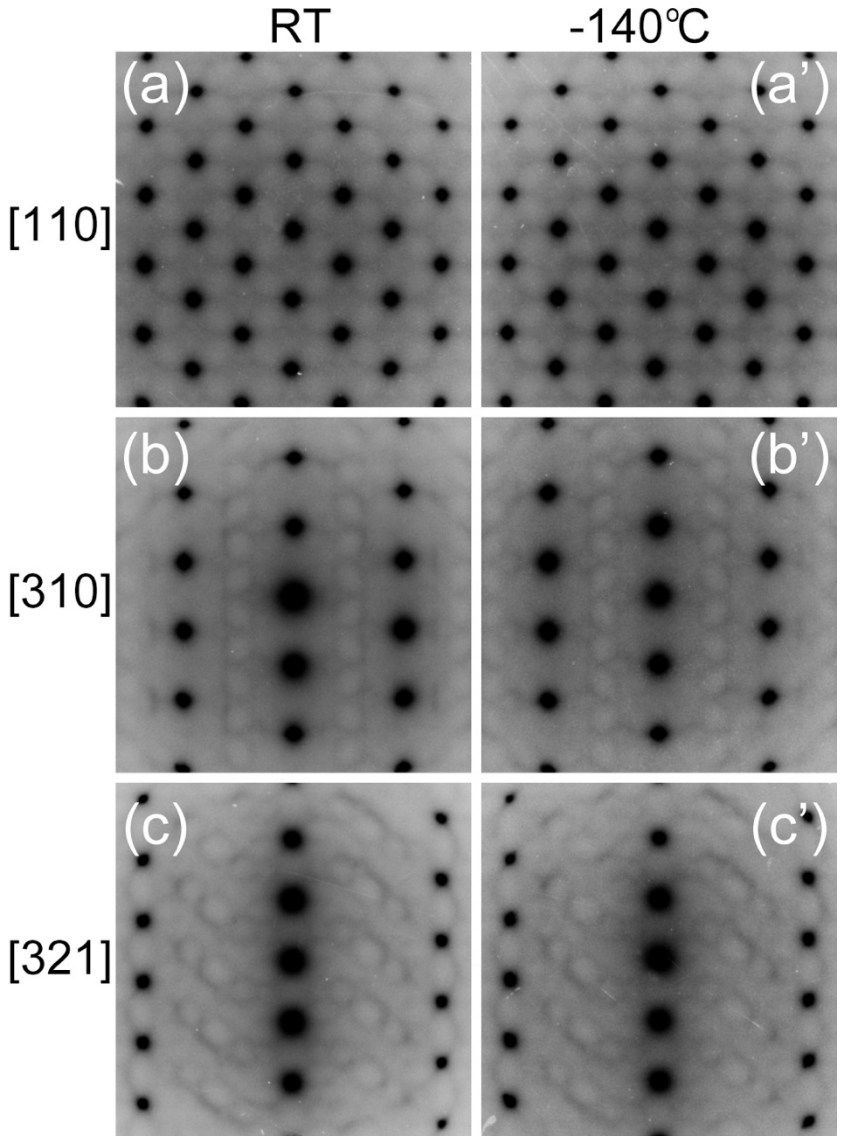

FIG. 7

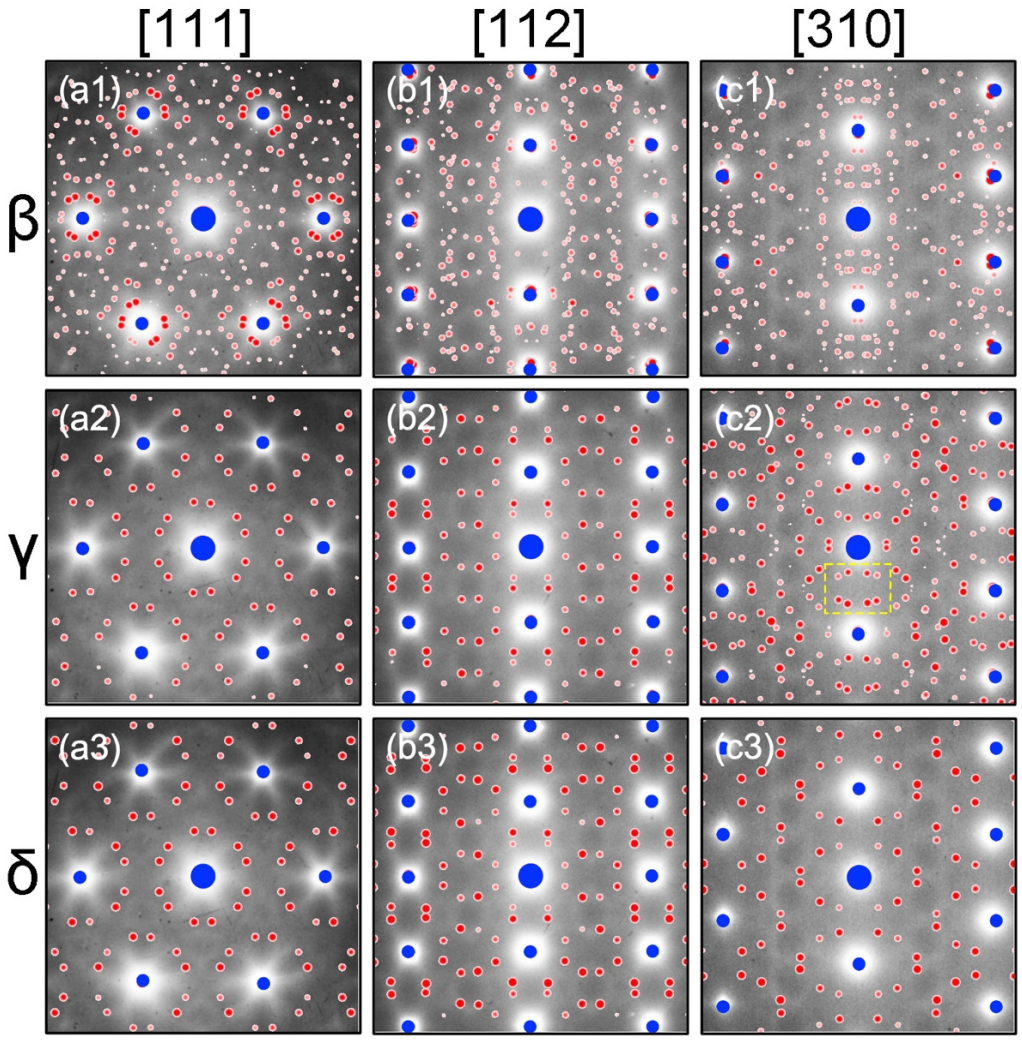

FIG. 8

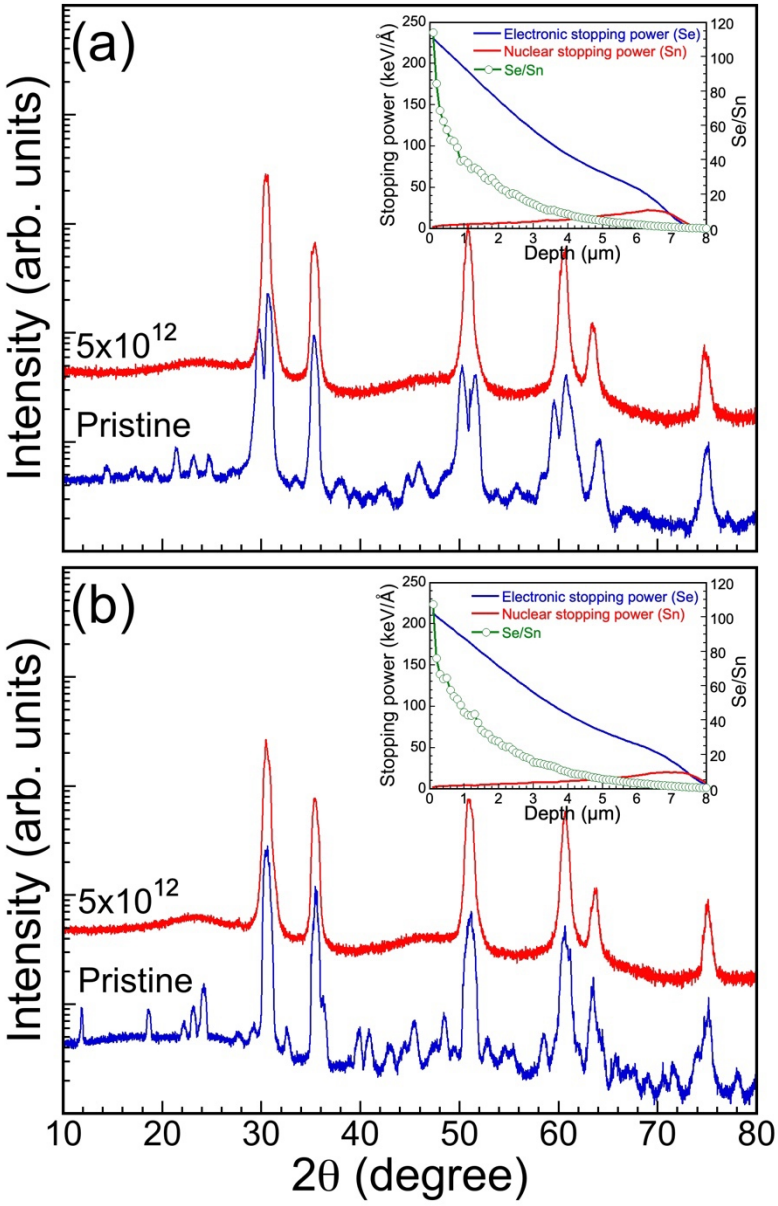
(a)
Intensity (arb. units)
5x10^12
Pristine
Electronic stopping power (Se)
Nuclear stopping power (Sn)
Se/Sn
Stopping power (keV/Å)
Depth (μm)
(b)
Intensity (arb. units)
5x10^12
Pristine
10 20 30 40 50 60 70 80
2θ (degree)

FIG. 9

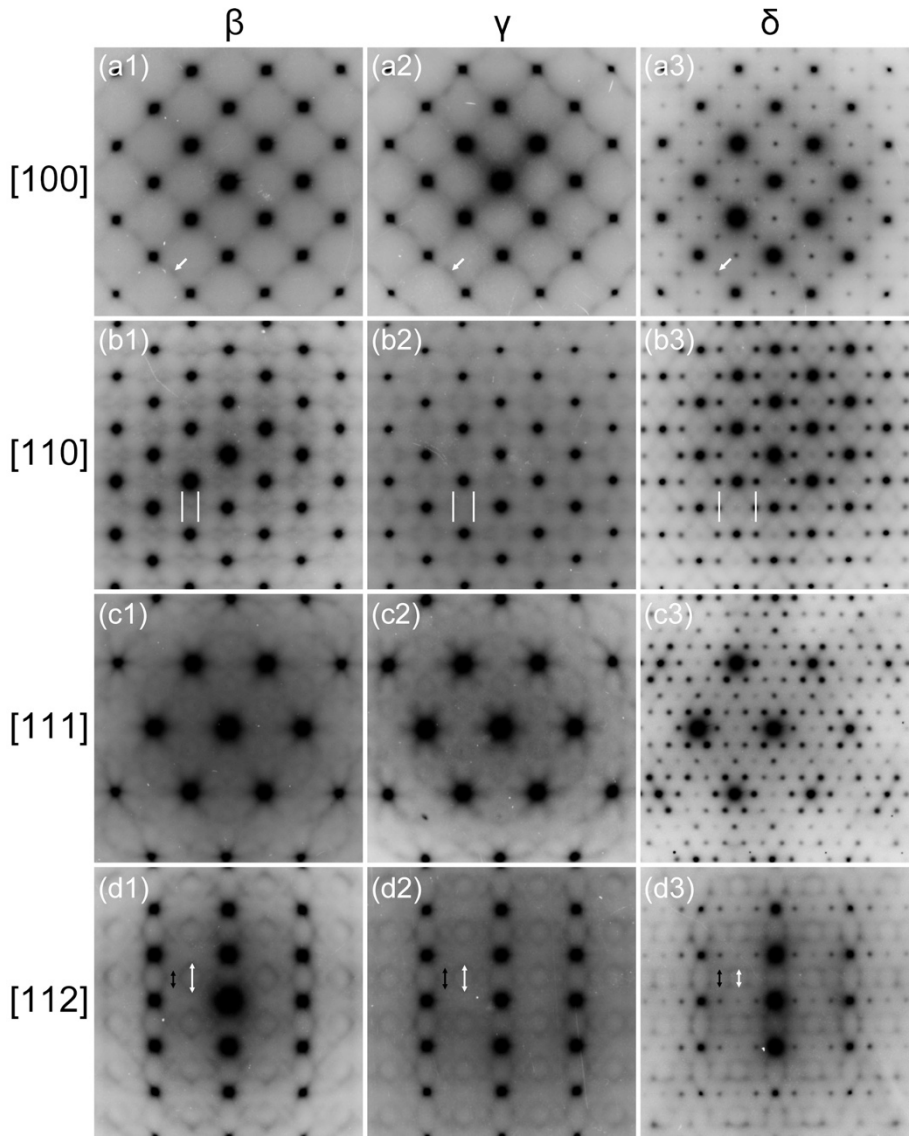

FIG. 10